Journal of Fluids and Structures 17 (2003) 261–274

JOURNAL OF FLUIDS AND STRUCTURES

www.elsevier.nl/locate/jnlabr/yjfls

Near-wake vortex motions behind a circular cylinder at low Reynolds number

J. Sung, J.Y. Yoo*

School of Mechanical and Aerospace Engineering, Seoul National University, San 56-1, Shinlim-dong, Kwanak-gu, Seoul 151-742, South Korea

Received 3 April 2001; accepted 16 August 2002

Abstract

A topological point of view is taken to investigate vortex motions in the near-wake region of a circular cylinder, where the Taylor hypothesis does not hold. Three-dimensional flow fields in the wake-transition regime are constructed by synthesizing time-resolved PIV data obtained in several planes of view. The convection velocities of the Kármán and secondary vortices are evaluated from the trajectories of the vortex center which is defined as the centroid of vorticity. Then, saddles are determined by applying the critical-point theory. It is shown that the inclination angle of the secondary vortices agrees well with previous experimental data. The flow fields in moving frames of reference have several critical points and the mushroom-like structure appears in the streamline patterns of the secondary vortices. Since the distributions of fluctuating Reynolds stresses defined by the triple decomposition are closely related to the existence of the secondary vortices, their physical interpretations are given in conjunction with the trajectories of the vortex center and saddle.

1. Introduction

Over the past decade, a considerable amount of work has been carried out on the coherent structures in the near wake of a circular cylinder for laminar, transitional and turbulent flows. They have been constantly of great research interest because even at low Reynolds numbers, of the order of a few hundred, the flow has three-dimensional structures. Until the shear layer vortices are formed at the Reynolds number above 1000, the flow field is referred to as wake-transition regime, where the secondary vortices with a spanwise wavelength of about one cylinder diameter appear (Williamson, 1996a). Considering that three dimensionality is introduced in the near-wake region by some flow instability, it is of great importance to observe the topological features of the structures in this region.

Most of previous experimental approaches to these structures have been made via flow visualization and point measurements (Williamson, 1996a; Gerrard, 1978; Wei and Smith 1986; Wu et al., 1994). However, flow visualization does not provide quantitative data and sometimes can be misleading because the rolling up of a streakline may not constitute a positive identification of the presence of discrete vortices (Hama, 1962; Gursul et al., 1990). The molecular diffusivities of the vorticity and markers being very different, vorticity should be expected to have diffused away from the smoke-marked fluid (Hussain, 1986). Further, the point measurement techniques such as hot-wire anemometry and LDV have limits in applying to complex flows in the near wake where the Taylor hypothesis does not hold.

Many efforts have been made to overcome the above limitations by utilizing multi-point or simultaneous measurements. Using scanning laser anemometer, Mansy, et al. (1994) investigated the streamwise vortices in the

*Corresponding author. Tel.: +82-2-880-7112; fax: +82-2-883-0179.
E-mail address: jyyoo@plaza.snu.ac.kr (J.Y. Yoo).
URL: http://eddy.snu.ac.kr.

0889-9746/03/$ - see front matter
PII: S0889-9746(02)00117-2

amplitude-modulated-velocity field by decomposing the flow into primary and secondary flow components. Lin et al. (1995b) and Brede et al. (1996) showed the spatio-temporal behavior of the streamwise vorticity component by acquiring time sequences of PIV images at a fixed streamwise position. Sung and Yoo (2001) reconstructed phase-averaged three-dimensional flow fields from the cinematic PIV data obtained in several planes of view. Some progresses have been made by these studies in analyzing the characteristics of the secondary vortices, but the topological structure and its relationship to the secondary vortices in the near wake still remain obscure to us.

Meanwhile, critical-point theory has been widely used to describe conceptually three-dimensional steady and unsteady flow patterns in an intelligible and unambiguous manner (Perry and Chong 1987). Critical points are those in the flow field where the velocity is zero relative to an appropriate observer and the streamline slope is indeterminate. Asymptotically exact solutions of the Navier-Stokes and continuity equations can be derived close to the critical points, which give a number of standard flow patterns. Perry and Chong (1987) and Chong et al. (1990) made a systematic classification of critical points that might be found in two- and three-dimensional flow fields. Hussain and Hayakawa (1987) discussed the role of vortex stretching at the saddle in turbulence production and mixing, by sampling conditionally coherent structures with a rake of eight X-wires. Zhou and Antonia (1994) obtained the flow topology and properties associated with critical points in the streamwise–spanwise and streamwise–transverse planes, by using an orthogonal array of 16 X-wires, and explained the three dimensionality of the organized motion with the inter-relationship between critical points simultaneously identified in the two planes. However, because these studies were on the basis of the Taylor hypothesis in the far wake, they cannot be applicable to the near wake where the vortical flow changes its shape and celerity three dimensionally.

Thus, a simultaneous multi-point measurement in more than two-dimensional space is necessary in the near wake. As one of the traditional measurement techniques in the turbulent flow, a flying-hot-wire apparatus synchronized with the reference phase signal was used by Cantwell and Coles (1983) who investigated transport processes in the near wake of a circular cylinder and explained the mechanism of turbulence production and entrainment near the critical points with the phase-averaged two-dimensional flow fields. Perry and Steiner (1987) discussed the topology of the phase-averaged velocity fields in the near wake of a normal flat plate in terms of the critical-point theory. Recently, with a rapid advance in PIV techniques, it is possible to identify directly the spatial disposition of the vortical structures. From instantaneous velocity fields, Wu et al. (1996b) observed statistical vortex patterns consistent with the evolution of the longitudinal vortices, and Lin et al. (1995a) made a physical interpretation of the turbulent near wake viewed from a fixed frame of reference by introducing topological concepts. When interpreting the onset of shear-layer vortices, Chyu and Rockwell (1996) addressed that flow topology of vorticity concentrations could be well defined by the instantaneous streamline patterns in moving frame of reference rather than in the laboratory frame.

The critical points are defined from the flow patterns viewed in a frame of reference translating with the vortices (Zhou and Antonia, 1994). Thus, the streamline patterns are sensitive to the choice of the velocity of the observer so that one topological pattern may change into another depending on the choice of the convection velocity (Perry and Chong, 1987). However, it is difficult to define the most appropriate convection velocity precisely, since the structures are developing with streamwise distance and different parts of the pattern are being convected at different velocities. Perry et al. (1980) and Perry and Tan (1984) calculated the convection velocities from the wavelength and frequency of the structures. Hussain and Hayakawa (1987) measured it by iteratively improving the time alignment which maximizes the cross-correlation of individual structure vorticity with the ensemble-averaged vorticity. Zhou and Antonia (1992) made a systematic study on the convection velocity measurements in a cylinder wake by classifying the techniques into two basic approaches. One is achieved by determining the velocity at the vortex center, and the other by estimating the time that a characteristic feature of the vortex travels a given distance. Nevertheless, these studies were confined to the flows compatible with the Taylor hypothesis. Earlier, Cantwell and Coles (1983) assumed that the convection velocity was given by the displacement history of the centroids of vorticiy and presented it for the Kármán vortex in the near wake. The present study follows their definition and obtains the convection velocities not only for the Kármán vortex but also for the secondary vortex.

The primary objective of the present study is to investigate the topological features of the near wake behind a circular cylinder in the frame of reference moving with the Kármán and secondary vortices, respectively. The secondary objective is to provide some insight into the role of critical points such as focus and saddle regarding the existence of the secondary vortices, by comparing the trajectories of them with the fluctuating Reynolds stress fields which are evaluated by subtracting the phase-averaged flow field from the instantaneous one. The three-dimensional flow fields in the wake-transition regime at a Reynolds number of 360 are constructed by synthesizing the time-resolved PIV data obtained in several planes of view, within which the vortex centers are located and the convection velocities of the vortices are estimated. In addition, the evolution of the secondary vortex filament is described in conjunction with the inclination angle.

2. Experimental setup

Experiments are conducted in a closed-cycle water tunnel with the size of the test-section, which is 15 cm wide, 10 cm high and 100 cm long. A circular cylinder is made of an acrylic plastic bar and placed horizontally across the test-section, which is 5 mm in diameter D, giving an aspect ratio of 30. The coordinate system is defined such that the origin is located at the center of the circular cylinder with x, y and z representing the streamwise, cross-stream (transverse) and spanwise directions, respectively. The measurement planes include one x–y and five z–x planes as shown in Fig. 1. These z–x planes lie below the cylinder axis at $y/D = 0$, -0.25, -0.5, -0.75 and -1, respectively. The flow information above the cylinder axis can be obtained by reflecting the velocity fields with a phase difference of 180° (Sung and Yoo 2001). The fields of view are $0<x<4.6D$ and $-2D<y<2D$ in the x–y plane, and $0.5D<x<4D$ and $0<z<2.9D$ in the z–x plane.

To measure the velocity field in the wake of a circular cylinder, hollow glass particles with a mean diameter of 10 μm and specific weight 1.1 are used to seed the flow. A time-resolved PIV system is used, where the particles are illuminated by a light sheet less than 1 mm in thickness, emitted from a 5-W argon-ion laser (Stabilite 2017, Spectra-Physics) and the scattered light is captured by a high-speed CCD camera (Hi-Dcam PCI 2000, NAC). This camera has an 8-bit sensor array of 480×420 pixels and can obtain images at a maximum speed of 250 frames/s with full resolution and 2000 frames/s with partial resolution (160×140 pixels). Continuous laser light is chopped by an electro-optic shutter (80X41, DANTEC) with a frequency response up to 50 kHz using a modulator crystal and a polarizer. This shutter can be triggered by a TTL signal and is synchronized with the camera using a programmable logic device (PLD). Velocity vectors are determined by cross-correlation analysis using fast fourier transforms (FFTs) with 32×32 pixels interrogation windows. To enhance the signal-to-noise ratio, window shifting technique is adopted and more detailed information can be found in our previous work (Sung and Yoo 2001). In the present study, a total of 2048 successive frames are acquired at 250 frames/s for one run, which produces 1024 velocity fields sampled at 125 Hz. This sample frequency is 40 times higher than the vortex shedding frequency obtained in the present application. For each measurement plane, four sets of 1024 successive velocity fields are acquired yielding a total of 4096 samples or more than 100 shedding cycles.

Velocity fields in the x–y and z–x planes are measured in the wake-transition regime at a Reynolds number of 360. The shedding frequency f_s is found to be 3.282 Hz and the corresponding Strouhal number is 0.204, which agrees quite well with the Strouhal–Reynolds number relationship presented by Roshko (1954) and Fey et al. (1998). From their curve fits, the Strouhal numbers are 0.2045 and 0.2025, respectively, at this Reynolds number. The spanwise wavelength

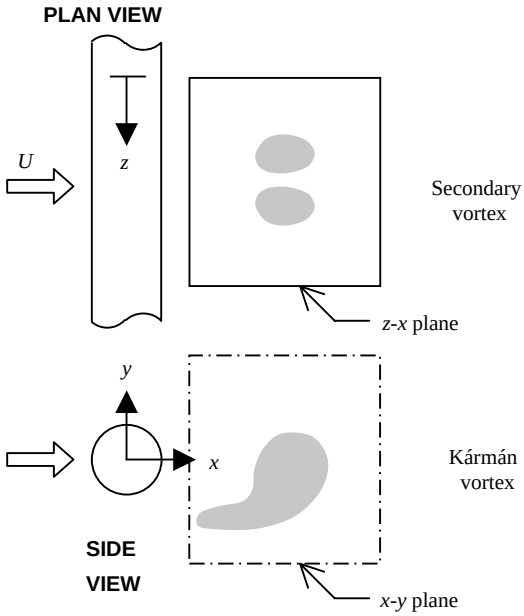

Fig. 1. Schematic of a three-dimensional field of view for vortex structures behind a circular cylinder.

obtained from the spatial correlation of the instantaneous vorticity (ω_y) distribution is about $0.93D$, which is also in good agreement with a previous experimental value (see Williamson, 1996b, Figure 14).

3. Phase-averaged structures in the near wake

Velocity signals in the wake-transition regime are periodic but include three-dimensional perturbations originated from the existence of the secondary vortices. This unsteady periodic velocity signal u can be viewed as a combination of a global mean component $\bar{u}$, a periodic mean component $\tilde{u}$, and a random component u' according to the triple decomposition (Hussain and Reynolds, 1970):

$$u(\vec{x},t) = \bar{u}(\vec{x}) + \tilde{u}(\vec{x},t) + u'(\vec{x},t) = \langle u(\vec{x},t)\rangle + u'(\vec{x},t),$$

$$\bar{u}(\vec{x}) = \lim_{T\to\infty} \frac{1}{T}\int_0^T u(\vec{x},t)\,\mathrm{d}t,$$

$$\langle u(\vec{x},t)\rangle = \lim_{N\to\infty} \frac{1}{N}\sum_{n=0}^{N-1} u(\vec{x},t+n\tau), \tag{1}$$

where τ is the shedding period and $\langle u\rangle$ is the phase average. As a reference signal for phase information the streamwise velocity at $(x/D,\ y/D) = (1.5, -0.5)$, which is low-pass filtered with a cut-off frequency set to be twice the shedding frequency, is used for the phase average by assigning the zero phase to each of the positive peaks. Then, the velocity fields in the x–y plane at a given phase are sampled in order to produce a representation of the phase-averaged structure of the Kármán vortices. Meanwhile, for the z–x planes, the vortex offset technique proposed by Sung and Yoo (2001) is applied to freeze the structure relative to the center-line of the measurement plane because a phase-averaging routine such as that for the x–y plane, which is widely used, does not give any structure due to the spanwise wandering of the secondary vortex. Fig. 2 shows a flow visualization result obtained in the z–x plane at $y/D = -0.5$, which reveals well the existence of the secondary vortices.

In the z–x planes except for the plane at $y/D = -0.5$, however, the reference phase signal is not included. Thus, the spanwise-averaged streamwise velocity at $x/D = 1.5$ in each plane takes the place of the reference signal assigning phases in a like manner. Note that all of these signals have phase-lags relative to the reference signal. To synchronize the phase in each z–x plane, the amount of phase-lag relative to the signal at $y/D = -0.5$ is calculated from the phase-averaged velocity field in the x–y plane, with which the phases in the z–x planes are compensated. Accordingly, a phase-locked three-dimensional flow field is reconstructed from the averaged data in five z–x planes.

A detailed description of the temporal behavior of the three-dimensional structure can be found in our previous work (Sung and Yoo, 2001, Figs. 8 and 9). Here, we only recall the reconstructed flow field for further analysis on flow

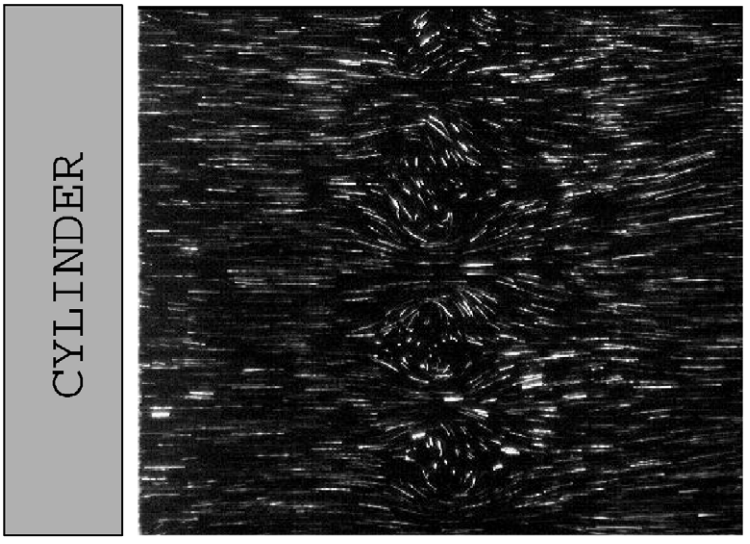

Fig. 2. Flow visualization of the secondary vortices in the z–x plane at $y/D = -0.5$. The flow direction is from left to right.

topology in the near wake. Fig. 3(a) shows the three-dimensional dispositions of the secondary vortices at phase 0°, which are forming a vortex filament. In this plot, the left and right iso-vorticity surfaces of the secondary vortices, which represent positive and negative values, respectively, configure to a vortex pair counter-rotating with respect to each other. To examine the spatial relation between the primary Kármán and secondary vortices, the structure in Fig. 3(a) is cut by an x–y plane, where the maximum positive value occurs, and overlapped with the Kármán vortices as is shown in Fig. 3(b). The solid/dashed line contours mark the vorticity levels of the Kármán vortex and the shaded contours represent those of the secondary vortex in the x–y plane. Note that a secondary vortex filament exists along the interface of the two consecutive Kármán vortices shed at different sides, which agrees with the schematic models of Williamson (1996a) and Brede et al. (1996).

4. Vortex centers and convection velocities

In the far wake of bluff bodies, the convection velocity of coherent structure is nearly constant but it is not so in the near wake because the structures are being developed in the streamwise direction. Therefore, in order to determine the convection velocity in the near wake, the locations of the vortex center should be traced along this direction. There are two possible definitions of the vortex center: one is the peak position of the vorticity and the other is the centroid of the vorticity field. The former is easy to realize but may result in high uncertainty. In the present study, the latter proposed by Cantwell and Coles (1983) is used with the centroid evaluated in the x–y plane as follows:

$$\Gamma = \int_A \langle \omega_z \rangle \, \mathrm{d}A,$$

$$x_c = \frac{1}{\Gamma} \int_A x \langle \omega_z \rangle \, \mathrm{d}A,$$

$$y_c = \frac{1}{\Gamma} \int_A y \langle \omega_z \rangle \, \mathrm{d}A, \tag{2}$$

where Γ is the circulation and A is the integration area which is restricted to the outside of the reversed-flow region, i.e., $x/D > 1.71$, since not a single vortex can be found in the inside. The summations in each case are allowed only for values of $\langle \omega_z \rangle / \langle \omega_z \rangle_p > 0.5$ to avoid relatively noisy data, where $\langle \omega_z \rangle_p$ is the maximum vorticity in the near-wake region.

Fig. 4 shows the temporal histories of the streamwise and cross-stream positions of the Kármán vortex center, where two different procedures to extract vortex centers by finding the peaks of the vorticity are compared. Note that the peak positions obtained from the phase-averaged flow field are more scattered than those obtained from the instantaneous flow field and averaged at constant phase. The scattering of the data from the phase-averaged flow field seems to be caused by the vortex separation and the local-peak movement. On the other hand, the averaged peak positions obtained from the instantaneous flow field are continuous, although they differ slightly from the positions of the centroid due to

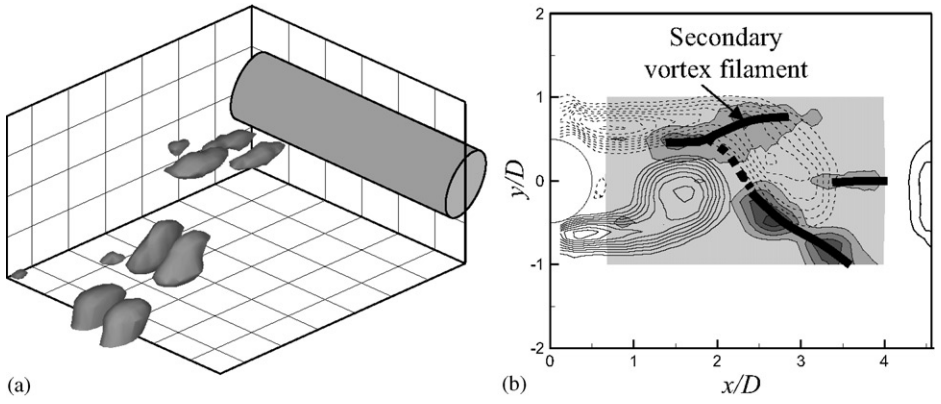

Fig. 3. Evolution of the three-dimensional structure. (a) Iso-vorticity surfaces of the secondary vortex. The left and right surfaces correspond to $\omega_y/(U/D) = 0.15$ and -0.15, respectively. (b) Spatial relation between the Kármán (ω_z) and secondary (ω_y) vortices. The solid/dashed line contours correspond to $\omega_z/(U/D)$ with minimum level 0.2 and increment 0.1. The shaded contours correspond to $\omega_y/(U/D)$ with minimum level 0.08 and increment 0.08.

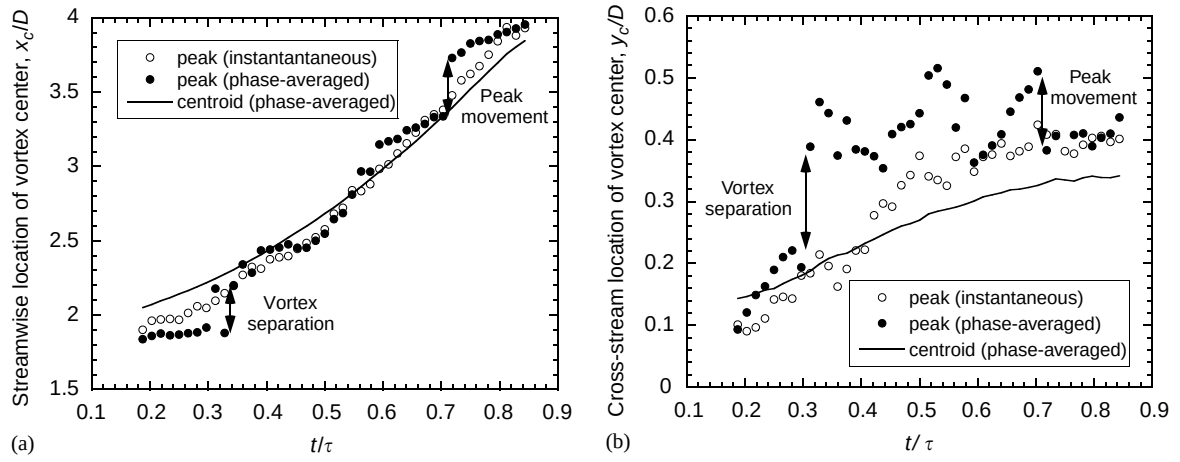

Fig. 4. Streamwise and cross-stream locations of the Kármán vortex center for different definitions: (a) x_c/D, (b) y_c/D.

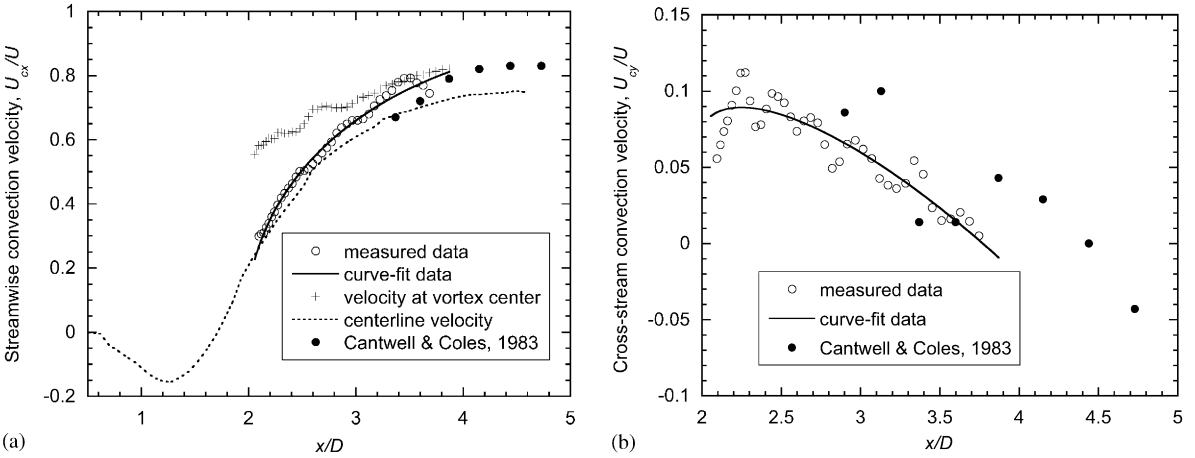

Fig. 5. Convection velocities of the Kármán vortex, which are obtained by differentiating the measured and curve-fit data of the centroid locations: (a) U_{cx}/U, (b) U_{cy}/U.

the eccentric shape of the Kármán vortex. However, the vortex centers defined by the centroid remain the same, independent of the two extracting procedures. Since a vortex can be thought as a rotational flow, it seems reasonable to assume the centroid of vorticity to be the center of rotation.

In Fig. 5, the streamwise and cross-stream convection velocities of the Kármán vortex calculated from the trajectories of the centroid are shown. The abscissa represents the streamwise position of the centroid at a given time. On the whole, the velocities obtained by differentiating the measured data directly (open circle) and those by differentiating the curve-fit functions (solid line) do not differ significantly. In addition, the present data show a trend similar to the experimental data of Cantwell and Coles (1983) although there are some discrepancies due to the difference in the Reynolds numbers. In Fig. 5(a), the streamwise convection velocity is compared with the long-time averaged velocity along the center-line. The two velocities are in close agreement in the upstream region but the convection velocity is slightly larger than the center-line velocity in the downstream region. Nevertheless, they seem to converge to certain values in the downstream region. Meanwhile, the velocity at the vortex center (cross-marker), which was used as the convection velocity by Zhou and Antonia (1992) based on the assumption of the Taylor hypothesis, considerably differ from the rest. The main reason for this is that, unlike a rigid body motion, the local fluid may slip off the bulk fluid, resulting in the change of the shape of the vortical structure. As the convection velocity becomes constant near $x = 4D$, it approaches the velocity at the vortex center. Thus, it can be inferred that these velocities will be the same in the far wake. The cross-stream

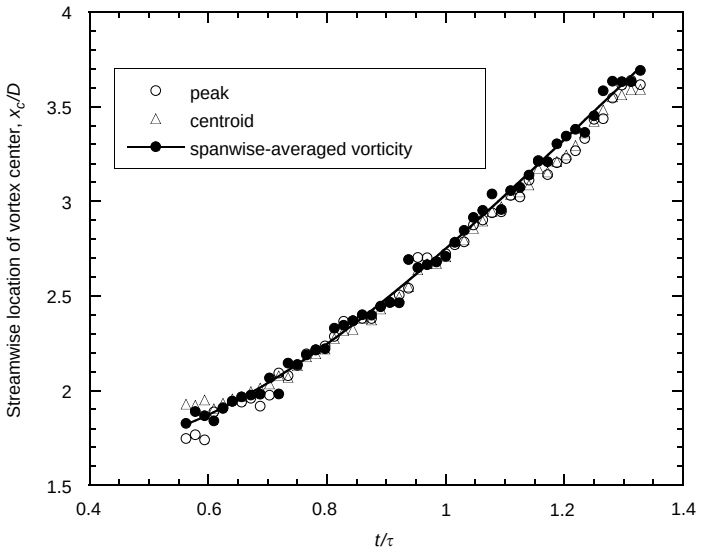

Fig. 6. Comparison of schemes to extract the secondary vortex center in the z–x plane at $|y/D| = 0.5$.

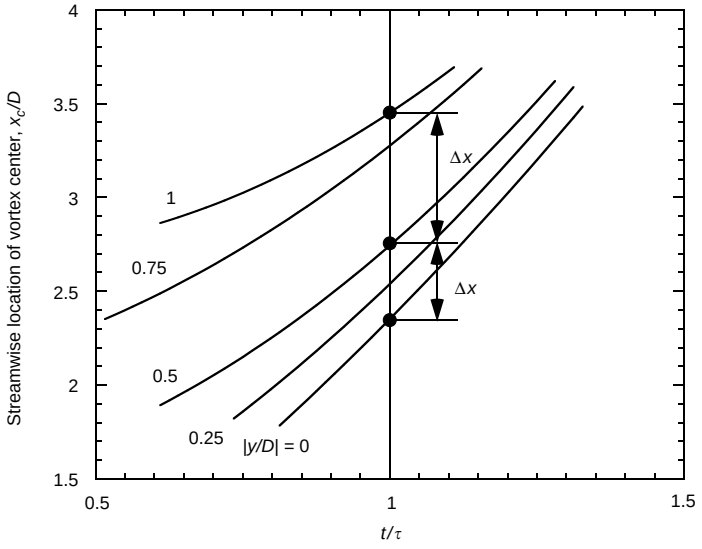

Fig. 7. Streamwise locations of the secondary vortex center in the z–x planes at various cross-stream positions.

convection velocity shown in Fig. 5(b) is, as expected, much smaller than the streamwise convection velocity, which increases at first and then decreases.

To see the effect of definitions for the secondary vortex centers, the trajectories of the vortex centers in the z–x plane at $y/D = -0.5$ are compared in Fig. 6. Unlike the Kármán vortices, the vortex centers defined by the peak and centroid of vorticity are identical since the vorticity field has a simple and concentric feature (see Fig. 11). Another definition in which the center is defined as a peak in the spanwise-averaged vorticity was given by Wu et al. (1996b), which also seems to be consistent with the others. Thus, all of the three definitions are considered to be appropriate for applying to the secondary vortices. In Fig. 7, the trajectories of the secondary vortex center in the five z–x planes are plotted, where the last scheme is applied and all the data are shown in the form of curve-fit functions. At a fixed time, the line connecting the vortex centers at separated cross-stream positions configures to a vortex filament and the difference of streamwise positions (Δx) between two cross-stream positions (Δy) gives an inclination angle of the secondary vortex filament as $\theta = \tan^{-1}(\Delta y/\Delta x)$. Fig. 8 shows the variations of the inclination angles obtained in the regions of $|y/D| = 0$–0.5 and

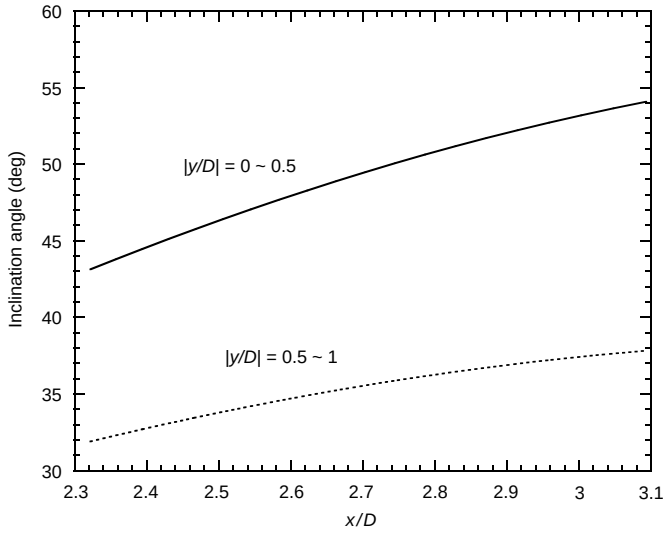

Fig. 8. Variation of the inclination angle of the secondary vortex filament along the streamwise position.

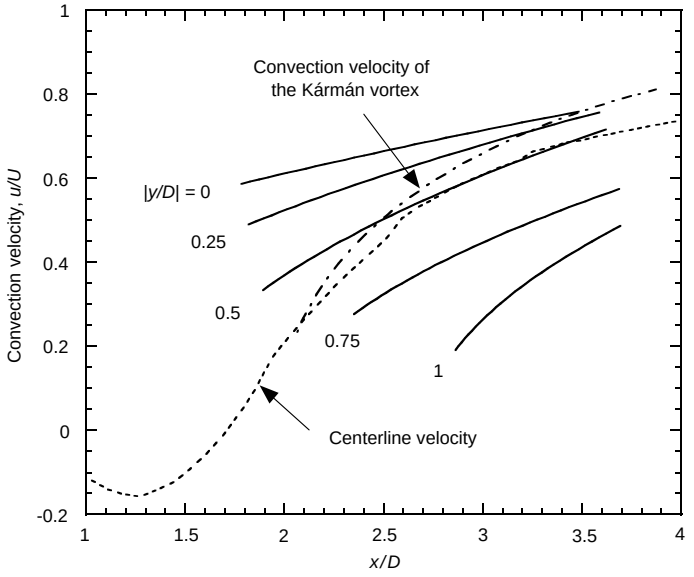

Fig. 9. Convection velocities of the secondary vortex in the z–x planes at various cross-stream positions.

0.5–1. In this plot, the abscissa denotes the streamwise position of the secondary vortex center at $|y/D| = 0.5$. On the whole, the angle increases as the vortex travels downstream and the vortex filament is inclined more sharply in the inner part than in the outer part. Wu et al. (1996b) found, using PIV, the inclination angle to be $47 \pm 9^\circ$ in the region of $|y/D| = 0$–0.53 and $x/D = 2.6$–5.4, which agrees well with the present result. Earlier, Hayakawa and Hussain (1989) suggested that the vortex filament was inclined at an angle of 60° to the x-axis in the far wake ($x/D > 20$), from their measurements using hot-wire anemometry, which is not contrary to the present result considering the increasing angle downstream.

In the same manner as that for the Kármán vortex, the convection velocities of the secondary vortices are evaluated at various cross-stream positions and compared with those of the Kármán vortex. As shown in Fig. 9, there are significant discrepancies among the convection velocities immediately after the secondary vortices are formed, and the closer the plane is to the center-line, the faster the secondary vortex is convected. On the other hand, in the downstream

region, all the velocities are gradually gathered around a certain value, which is comparable to the convection velocity of the Kármán vortex. To sum up, as a secondary vortex filament moves downstream in the near wake, it is more and more inclined to the x-axis with the inner part moving faster and the outer part moving slower than its global translating velocity.

5. Sectional topology in moving frame of reference

The most essential requirement for analyzing the three-dimensional topology in the cylinder wake is that all the velocity vectors are measured with a sufficient sampling rate in the three-dimensional space. A holographic PIV system with a high sampling rate and a three-dimensional PTV with a high recovery ratio for extracting velocity vectors may be the most plausible candidates. However, these configurations are unreachable yet in the present state of the art. Instead, in the present study, we are to make an attempt to do this from a topological point of view. That is, we are to observe the sectional flow fields in the frame of reference moving at the convection velocity of the vortical structure in the x–y and z–x planes.

In Figs. 10 and 11, the velocity and vorticity fields, and the sectional streamlines in moving frames of reference are shown at phase 0° in the x–y and z–x planes, respectively. The vorticity distributions shown in Figs. 10(a) and 11(a) are invariant with the frame of reference. As mentioned earlier, the convection velocity in the near wake varies with the streamwise location of the vortices so that it can be represented as a function of time. Thus, the velocity fields in the x–y plane shown in Fig. 10 can be represented at a given time as

$$u_c(x, y, t) = \langle u(x, y, t) \rangle - U_{cx}(t),$$

$$v_c(x, y, t) = \langle v(x, y, t) \rangle - U_{cy}(t). \tag{3}$$

The same procedure can be applied to the z–x plane in Fig. 11. In the streamline pattern of Fig. 10(b), some critical points such as focus and saddle are detected, which would not be clearly seen in a fixed frame of reference. Furthermore, in the z–x plane, the streamline pattern of Fig. 11(b) shows the existence of a node and a bifurcation line as well as the foci and saddles. Among these, a bifurcation line occurs when critical points merge, split or change type as their trajectories cross the boundaries between topological domains (Chong et al., 1990). Another interesting feature in the z–x plane is that the sectional streamlines describe well the mushroom-type structures frequently seen in previous flow visualization (Williamson, 1996a).

To examine the flow properties associated with critical points in the x–y plane, which will be discussed later, the locations of saddles are evaluated using the critical-point theory (Perry and Chong, 1987) for all consecutive times. If we recall the basic concepts of the theory, the velocity fields (u_c, v_c) in Eq. (3) can be approximated near a critical point

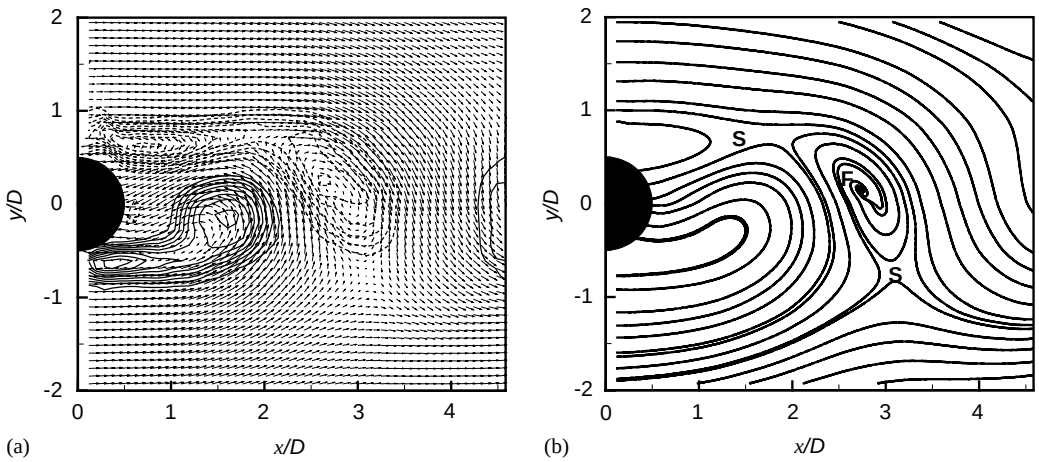

Fig. 10. Flow fields in the x–y plane at phase 0° viewed from a moving frame of reference: (a) velocity and vorticity fields, (b) streamlines. S, saddle; F, focus.

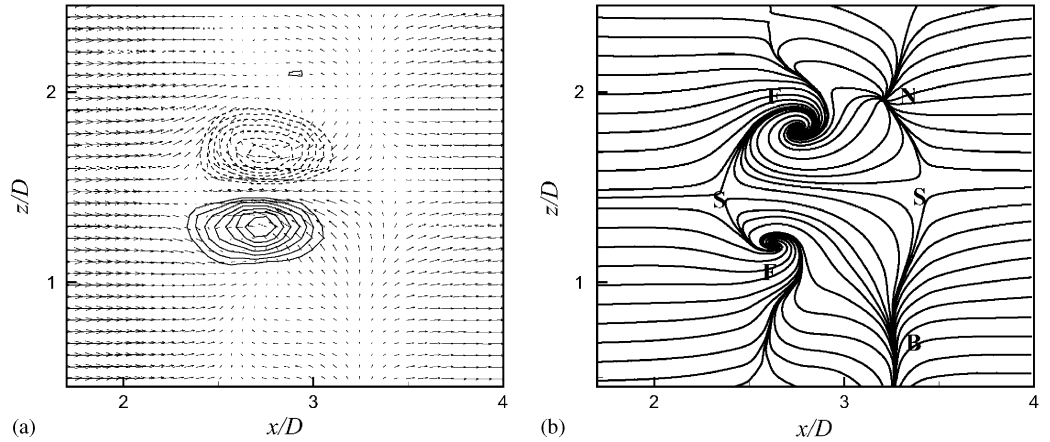

Fig. 11. Flow fields in the z–x plane at $y/D = -0.5$ viewed from a moving frame of reference at phase 0°: (a) velocity and vorticity fields, (b) streamlines. S, saddle; F, focus; N, node; B, bifurcation line.

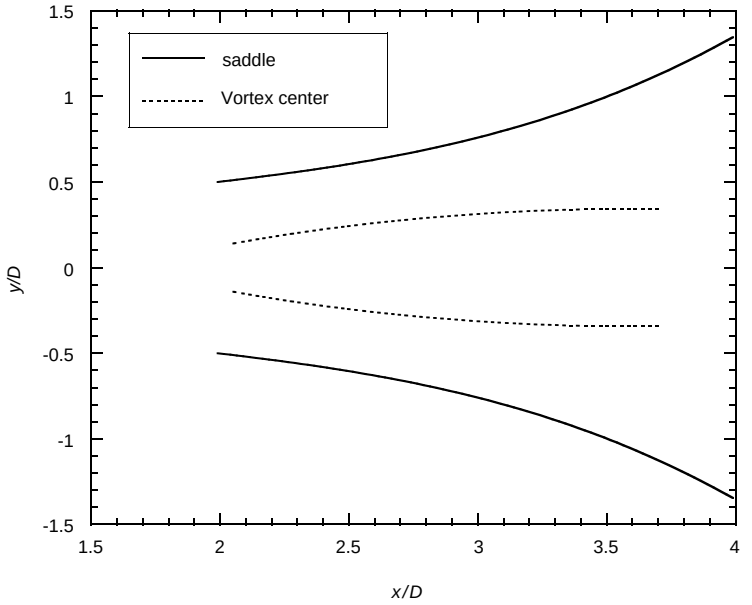

Fig. 12. Trajectories of the vortex center and saddle.

(x_c, y_c) by the Taylor series expansions as follows:

$$\begin{bmatrix} u \\ v \end{bmatrix} = \begin{bmatrix} a_{11} & a_{12} \\ a_{21} & a_{22} \end{bmatrix} \begin{bmatrix} x \\ y \end{bmatrix} = \mathbf{A} \begin{bmatrix} x \\ y \end{bmatrix},$$

$$a_{11} = \frac{\partial u}{\partial x}, \quad a_{12} = \frac{\partial u}{\partial y}, \quad a_{21} = \frac{\partial v}{\partial x}, \quad a_{22} = \frac{\partial v}{\partial y}. \tag{4}$$

Critical points are classified according to the eigenvalues of matrix **A** by various types such as saddle, node and focus. Among these, saddle occurs when the determinant of matrix **A** is less than 0. Since the velocity is zero at critical points, the location of a critical point is determined by searching for the minimum of $f = (u^2 + v^2)^{1/2}$. Once a critical point is located, the determinant is calculated to judge whether it is a saddle or not. In Fig. 12, the resultant trajectory of the

saddle is compared with that of the vortex center obtained earlier. At first, the vortex center moves away from the center-line and is then kept at a constant distance, while the saddle continuously moves away from the center-line.

6. Incoherent reynolds stress associated with critical points

The development of three-dimensional instabilities and the formation of the secondary vortices in the cylinder wake induce velocity perturbations to the velocity signals and result in a velocity spike (Wu et al., 1996a). From the viewpoint of phase averaging, the phase mean is associated with coherent large-scale structure, while the velocity fluctuation away

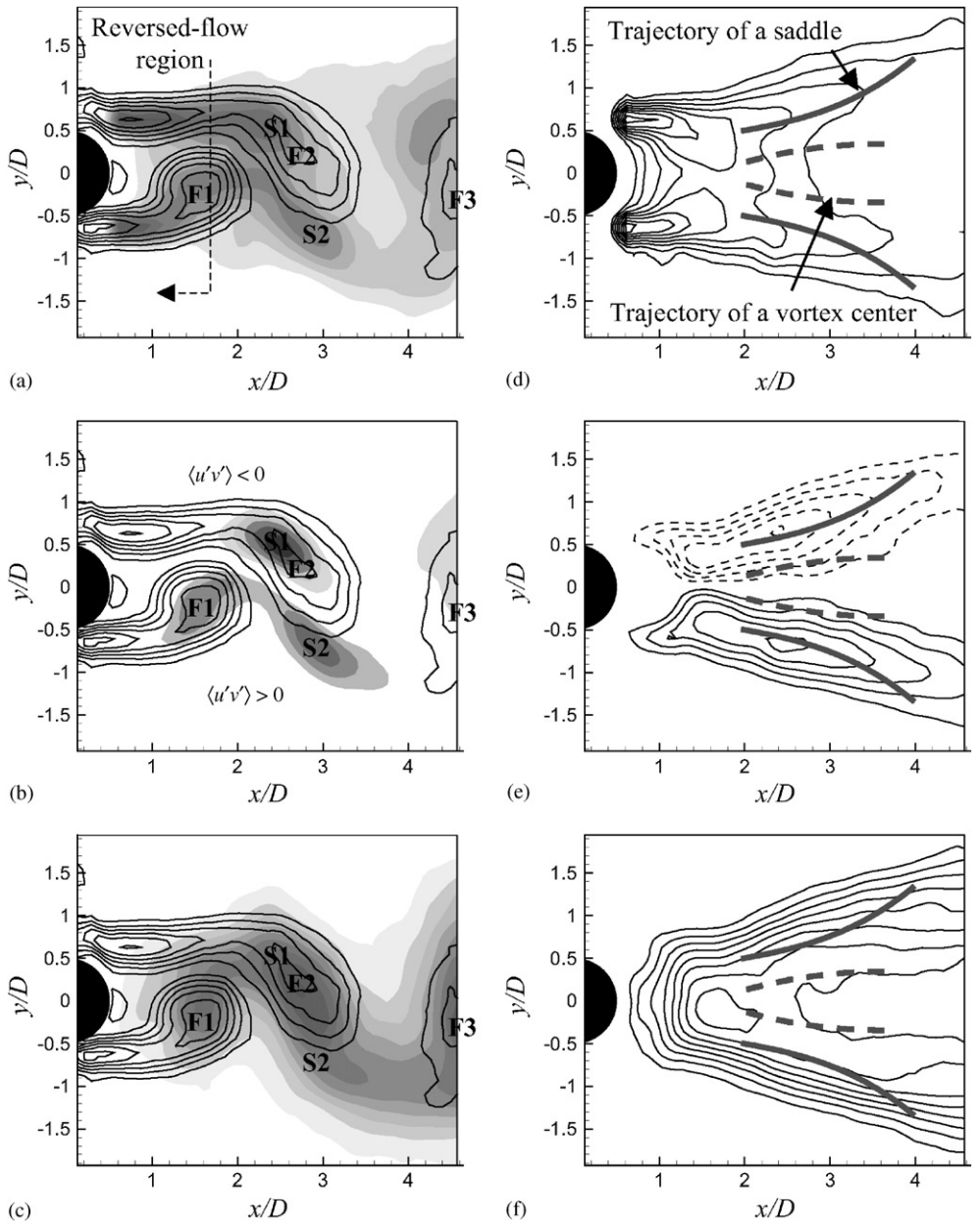

Fig. 13. Contours of fluctuating Reynolds stress components: in the left plots, the line contours represent vorticity fields and the shaded contours represent (a) $\langle u'u' \rangle$, (b) $\langle u'v' \rangle$, (c) $\langle v'v' \rangle$, which are ensemble-averaged quantities at phase 0°. In the right plots, the line contours represent (d) $\overline{\langle u'u' \rangle}$, (e) $\overline{\langle u'v' \rangle}$, (f) $\overline{\langle v'v' \rangle}$, which are time-averaged quantities.

from the mean comes from incoherent small-scale random turbulence or dispersion of large-scale motions. Most of all, the fluctuating Reynolds stresses play an important role in the momentum transport equation for the mean flow at constant phase [see Cantwell and Coles, (1983), Equation (5)]. It means that these stresses directly control the dynamics of the coherent structures and operate as local phenomena. Thus, in the present study, the distributions of the fluctuating Reynolds stresses are considered in the x–y plane by relating them with the critical points as shown in Fig. 13. In the left plots of Fig. 13, the line contours represent the vorticity fields and the shaded contours represent the fluctuating Reynolds stress components which are obtained from the random components of Eq. (1) and then ensemble averaged at phase 0°. The number of realizations for the ensemble average is about 100 and the error of the averaged value is within 8% for a 95% confidence limit according to the uncertainty analysis made by Hitching and Lewis (1999). Since there are two distinct Kármán vortices, each saddle–focus system of S1–F1 or S2–F2 is located in a frame of reference moving with the convection velocity of the corresponding vortex. These figures show that $\langle u'u' \rangle$ is concentrated near the vortex center in the reversed-flow region but near the saddle downstream of that region. On the whole, $\langle u'v' \rangle$ is negative above the center-line and positive below the center-line and the local maximum of its absolute value lies in the saddle region. While, $\langle v'v' \rangle$ has its maxima at the vortex center and is concentrated along the curve connecting the positions of vortex centers. This fact can be confirmed from the distributions of time-averaged fluctuating Reynolds stresses as shown in Figs. 13(d–f), where the trajectories of the vortex center and saddle are overlapped. A total of 4096 data are involved in the time average and the estimated error is less than 1%. Regarding $\overline{\langle u'u' \rangle}$, its peak is found in the reversed-flow region and then it gradually decreases but has a slightly larger value along the trajectory of the saddle if it is observed at a fixed streamwise position. Surely, the maximum concentration of $\overline{\langle u'v' \rangle}$ exists along the trajectory of the saddle. On the contrary, $\overline{\langle v'v' \rangle}$ is thought to be closely related with the trajectory of the vortex center since it is concentrated around the center-line.

Now, we are to discuss the physical meaning of the fluctuating Reynolds stress fields regarding the spatial disposition of the secondary vortex filament. In Fig. 14, the sectional streamlines viewed from a moving frame of reference in the x–y plane are overlapped with the vorticity distributions of the secondary vortex (shaded contours) at phase 0°. It is noted that the diverging separatrix of the saddle is aligned with the vortex filament, making the filament stretch along the diverging separatrix. During the process of vortex stretching, the surrounding fluid is advected to the saddle along the converging separatrix, which produces large velocity fluctuations. The inclination of the vortex filament and the rapid flux of x-momentum toward the filament generate a positive correlation between u' and v' in the saddle region, irrespective of the direction of circulation in the filament. Thus, $\langle u'v' \rangle$ has a higher positive value in the saddle region below the center-line. On the other hand, due to the strong rotational fluid motion around the vortex center, $\langle u'u' \rangle$ and $\langle v'v' \rangle$ have somewhat larger amplitudes near the center. However, comparably large x-momentum flux in the saddle region makes $\langle u'u' \rangle$ a little bit higher at the saddle than at the vortex center downstream of the reversed-flow region.

Although three-dimensional streamlines cannot be drawn from lack of information on the y-component of the velocity along the z-axis in the present measurements, some qualitative interpretations are possible as sketched in Fig. 15 with the following hypothesis. From Fig. 14, the saddle in the x–y plane seems to be located just upstream of the secondary vortices when one considers a plane normal to the page and containing the saddle. Thus, the spanwise

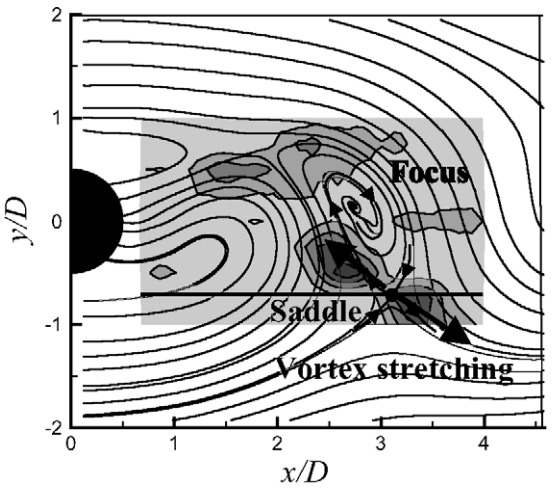

Fig. 14. Streamlines and vorticity contours of the secondary vortex (ω_y) at phase 0° viewed from a moving frame of reference.

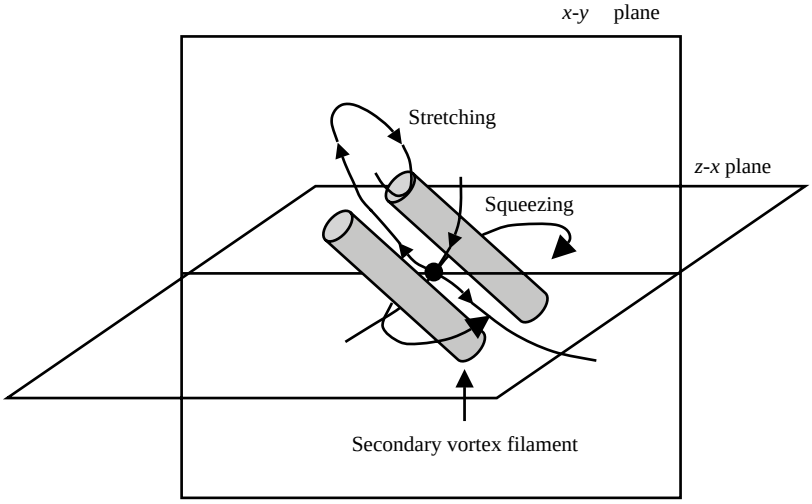

Fig. 15. Schematic model of the three-dimensional streamline around a saddle. There are two diverging separatrices. One of them stretches vortex filament and the other squeezes the filament.

position of the saddle in Fig. 14 is thought to approximately coincide with that of the upstream saddle of the secondary vortices in Fig. 11(b). The schematic model in Fig. 15, representing streamlines around a saddle in a frame of reference moving with the vortices, shows that one diverging separatrix of a saddle squeezes the filaments while they are stretched in the opposite directions along another diverging separatrix.

7. Concluding remarks

The velocity fields in near wake behind a circular cylinder are measured by a time-resolved PIV in several planes of view and the phase-locked three-dimensional structure is presented by reconstructing the flow fields from phase-averaged data. From the evolution process of the structure, it is noted that a vortex filament found between consecutive Kármán vortices is formed alternately at the lower and upper sides of the cylinder, sequentially attached to the newly formed one and detached from the previously linked one. To investigate the flow topology in a moving frame of reference, appropriate schemes to determine the vortex center and convection velocity should be selected. Consequently, it proves to be reasonable to use the centroid of the vorticity as the vortex center. In the near wake, it is suggested that the convection velocity be derived from the trajectory of the vortex center rather than the velocity at the vortex center.

A secondary vortex filament inclined to the x-axis is convected with the inner part moving faster and the outer part moving slower. The overall inclination angle of the secondary vortex filament, known from the spatial disposition of the center, agrees well with the previous results. The resultant flow fields viewed from moving frames of reference have several critical points, and the sectional streamlines around the secondary vortices describe the mushroom-type structure very well. Further, the trajectory of the saddle is estimated quantitatively, based on the critical-point theory. The fluctuating Reynolds stress fields associated with the vortex center and saddle lead to interesting flow phenomena. The diverging separatrix of a saddle aligned with the secondary vortex filament results in vortex stretching, which makes $\langle u'v' \rangle$ dominant in the saddle region. Due to the strong rotational focus at the center, $\langle u'u' \rangle$ and $\langle v'v' \rangle$ have larger amplitudes in this region but are more affected by the large momentum flux in the saddle region.

Acknowledgements

This work was supported by the Brain Korea 21 Project, Ministry of Education, Republic of Korea.

References

Brede, M., Eckelmann, H., Rockwell, D., 1996. On secondary vortices in the cylinder wake. Physics of Fluids 8, 2117–2124.

Cantwell, B., Coles, D., 1983. An experimental study of entrainment and transport in the turbulent near wake of a circular cylinder. Journal of Fluid Mechanics 136, 321–374.

Chong, M.S., Perry, A.E., Cantwell, B.J., 1990. A general classification of three-dimensional flow fields. Physics of Fluids A 2, 765–777.

Chyu, C., Rockwell, D., 1996. Near-wake structure of an oscillating cylinder: effect of controlled shear-layer vortices. Journal of Fluid Mechanics 322, 21–49.

Fey, U., König, M., Eckelmann, H., 1998. A new Strouhal-Reynolds-number relationship for the circular cylinder in the range $47 < \mathrm{Re} < 2 \times 10^5$. Physics of Fluids 10, 1547–1549.

Gerrard, J.H., 1978. The wakes of cylindrical bluff bodies at low Reynolds number. Philosophical Transactions of the Royal Society of London, Series A 288, 351–382.

Gursul, I., Lusseyran, D., Rockwell, D., 1990. On interpretation of flow visualization of unsteady shear flows. Experiments in Fluids 9, 257–266.

Hama, F.R., 1962. Streaklines in a perturbed shear flow. The Physics of Fluids 5, 644–650.

Hayakawa, M., Hussain, F., 1989. Three-dimensionality of organized structures in a plane turbulent wake. Journal of Fluid Mechanics 206, 375–404.

Hitching, E., Lewis, A.W., 1999. Sampling techinques for accurate measurement of Reynolds stresses using laser Doppler anemometry. Flow Measurement and Instrumentation 10, 241–247.

Hussain, A.K.M.F., 1986. Coherent structures and turbulence. Journal of Fluid Mechanics 173, 303–356.

Hussain, A.K.M.F., Hayakawa, M., 1987. Eduction of large-scale organized structures in a turbulent plane wake. Journal of Fluid Mechanics 180, 193–229.

Hussain, A.K.M.F., Reynolds, W.C., 1970. The mechanics of an organized wave in turbulent shear flow. Journal of Fluid Mechanics 41, 241–258.

Lin, J.-C., Towfighi, J., Rockwell, D., 1995a. Instantaneous structure of the near-wake of a circular cylinder: on the effect of Reynolds number. Journal of Fluids and Structures 9, 409–418.

Lin, J.-C., Vorobieff, P., Rockwell, D., 1995b. Three-dimensional patterns of streamwise vorticity in the turbulent near-wake of a cylinder. Journal of Fluids and Structures 9, 231–234.

Mansy, H., Yang, P.-M., Williams, D.R., 1994. Quantitative measurements of three-dimensional structures in the wake of a circular cylinder. Journal of Fluid Mechanics 270, 277–296.

Perry, A.E., Chong, M.S., 1987. A description of eddying motions and flow patterns using critical-point concepts. Annual Review of Fluid Mechanics 19, 125–155.

Perry, A.E., Lim, T.T., Chong, M.S., 1980. The instantaneous velocity fields of coherent structures in coflowing jets and wakes. Journal of Fluid Mechanics 101, 243–256.

Perry, A.E., Steiner, T.R., 1987. Large-scale vortex structures in turbulent wakes behind bluff bodies. Part 1. Vortex formation processes. Journal of Fluid Mechanics 174, 233–270.

Perry, A.E., Tan, D.K.M., 1984. Simple three-dimensional vortex motions in coflowing jets and wakes. Journal of Fluid Mechanics 141, 197–231.

Roshko, A., 1954. On the development of turbulent wakes from vortex streets. NACA Report 1191.

Sung, J., Yoo, J.Y., 2001. Three-dimensional phase-averaging of time-resolved PIV measurement data. Measurement Science and Technology 12, 655–662.

Wei, T., Smith, C.R., 1986. Secondary vortices in the wake of circular cylinders. Journal of Fluid Mechanics 169, 513–533.

Williamson, C.H.K., 1996a. Three-dimensional wake transition. Journal of Fluid Mechanics 328, 345–407.

Williamson, C.H.K., 1996b. Vortex dynamics in the cylinder wake. Annual Review of Fluid Mechanics 28, 477–539.

Wu, J., Sheridan, J., Soria, J., Welsh, M.C., 1994. An experimental investigation of streamwise vortices in the wake of a bluff body. Journal of Fluids and Structures 8, 621–625.

Wu, J., Sheridan, J., Welsh, M.C., 1996a. Velocity perturbations induced by the longitudinal vortices in a cylinder wake. ASME Journal of Fluids Engineering 118, 531–536.

Wu, J., Sheridan, J., Welsh, M.C., Hourigan, K., 1996b. Three-dimensional vortex structures in a cylinder wake. Journal of Fluid Mechanics 312, 201–222.

Zhou, Y., Antonia, R.A., 1992. Convection velocity measurements in a cylinder wake. Experiments in Fluids 13, 63–70.

Zhou, Y., Antonia, R.A., 1994. Critical points in a turbulent near wake. Journal of Fluid Mechanics 275, 59–81.